Supplementary Information for "Dynamics of $K_2Ni_2(SO_4)_3$ governed by proximity to a 3D spin liquid model"

Matías G. Gonzalez,[1,2] Vincent Noculak,[1,2] Aman Sharma,[3] Virgile Favre,[3] Jian-Rui Soh,[3] Arnaud Magrez,[4] Robert Bewley,[5] Harald O. Jeschke,[6,7] Johannes Reuther,[1,2,7] Henrik M. Rønnow,[3] Yasir Iqbal,[7] and Ivica Živković[3]

[1] *Helmholtz-Zentrum Berlin für Materialien und Energie, Hahn-Meitner-Platz 1, 14109 Berlin, Germany*
[2] *Dahlem Center for Complex Quantum Systems and Fachbereich Physik, Freie Universität Berlin, 14195 Berlin, Germany*
[3] *Laboratory for Quantum Magnetism, Institute of Physics, École Polytechnique Fédérale de Lausanne, CH-1015 Lausanne, Switzerland*
[4] *Crystal Growth Facility, École Polytechnique Fédérale de Lausanne, Lausanne, Switzerland.*
[5] *ISIS Pulsed Neutron and Muon Source, STFC Rutherford Appleton Laboratory, Harwell Science and Innovation Campus, Didcot, Oxfordshire, OX11 0QX UK*
[6] *Research Institute for Interdisciplinary Science, Okayama University, Okayama 700-8530, Japan*
[7] *Department of Physics and Quantum Centre of Excellence for Diamond and Emergent Materials (QuCenDiEM), Indian Institute of Technology Madras, Chennai 600036, India*

Supplementary Note 1. STRUCTURE OF $K_2NI_2(SO_4)_3$

The structure of $K_2Ni_2(SO_4)_3$ consists of a cubic cell of side $a = 9.81866$ Å containing 8 magnetic ions with $S = 1$. These ions can be separated into two symmetry-inequivalent groups of 4. Each group forms a trillium lattice whose positions are given in Supplementary Table 1 as a function of the parameter u. The parameters for the two trillium lattices are $u_1 = 0.33554$ and $u_2 = 0.59454$. Given these positions, the distance of the five-nearest-neighbour interactions are 4.405, 4.889, 6.072, 6.112, 6.114 Å, respectively. The fourth and fifth-nearest neighbours are exchanged compared to the room-temperature structure from Ref. [S1]. To avoid inconsistencies and confusion with previous articles, we rename the first five-nearest-neighbour interactions as J_1, J_2, J_3, J_5, and J_4 (note that the last two names are exchanged to keep the same nomenclature as in Ref. [S1]). These interactions are shown in Supplementary Fig. 1.

site	position
1	(u, u, u)
2	$\left(\frac{1}{2}+u, \frac{1}{2}-u, 1-u\right)$
3	$\left(1-u, \frac{1}{2}+u, \frac{1}{2}-u\right)$
4	$\left(\frac{1}{2}-u, 1-u, \frac{1}{2}+u\right)$

Supplementary Table 1. Positions of the four sites corresponding to a trillium lattice within the cubic unit cell. Every vector has to be multiplied by the size of the unit cell a to obtain the real positions.

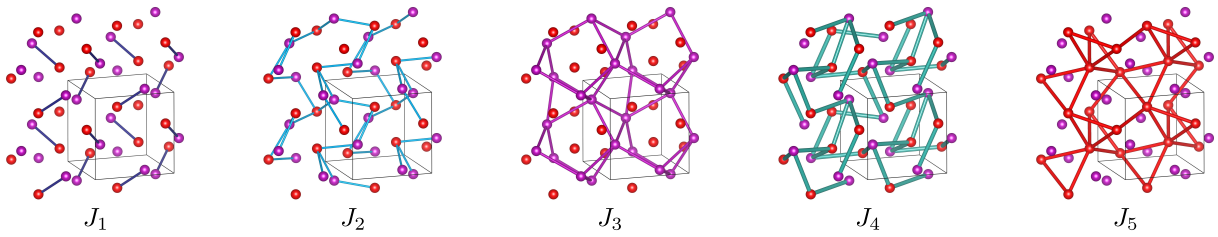

Supplementary Figure 1. Couplings corresponding to the first five nearest neighbours in the $K_2Ni_2(SO_4)_3$ structure.

Supplementary Note 2. DFT ENERGY MAPPING FOR THE LOW-TEMPERATURE STRUCTURE

The five nearest neighbour couplings used for the model of $K_2Ni_2(SO_4)_3$ are shown in Supplementary Fig. 1, and Supplementary Fig. 2 shows the result of the energy mapping procedure for 5 different values of the onsite interaction

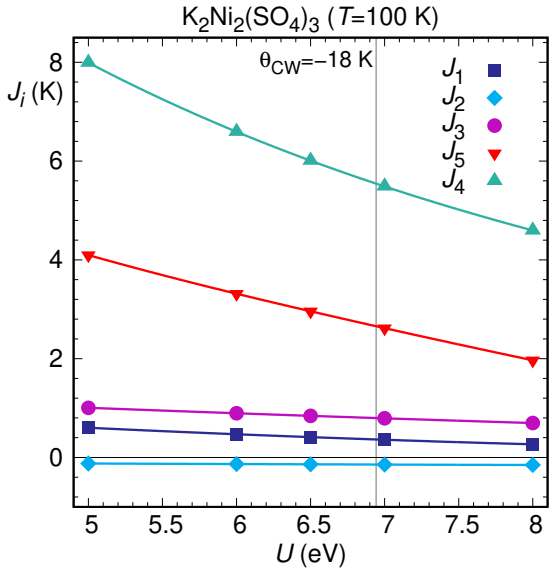

Supplementary Figure 2. DFT energy mapping for the $T = 100\,\mathrm{K}$ structure of $K_2Ni_2(SO_4)_3$ calculated with DFT+U as function of onsite interaction strength U. The Hund's rule coupling value is fixed at $J_\mathrm{H} = 0.88\,\mathrm{eV}$ [S2]. The vertical line indicates the U value where the couplings match the experimental Curie-Weiss temperature.

U (eV)	J_1 (K)	J_2 (K)	J_3 (K)	J_5 (K)	J_4 (K)	J_6 (K)	J_7 (K)	J_8 (K)	θ_{CW} (K)
5	0.602(2)	-0.123(1)	1.005(2)	4.097(1)	7.992(1)	0.025(1)	-0.012(1)	0.022(1)	-26.4
6	0.470(2)	-0.133(1)	0.895(1)	3.315(1)	6.594(1)	0.020(1)	-0.009(1)	0.018(1)	-21.7
6.5	0.412(2)	-0.139(1)	0.842(2)	2.960(1)	6.009(1)	0.0169(1)	-0.008(1)	0.016(1)	-19.7
6.942	**0.364(2)**	**-0.144(1)**	**0.798(2)**	**2.657(1)**	**5.545(1)**	**0.015(1)**	**-0.007(1)**	**0.014(1)**	**-18**
7	0.358(2)	-0.144(1)	0.792(2)	2.618(1)	5.487(1)	0.015(1)	-0.007(1)	0.014(1)	-17.8
7.5	0.312(1)	-0.148(1)	0.744(1)	2.289(1)	5.017(1)	0.012(1)	-0.007(1)	0.013(1)	-16.1
8	0.266(1)	-0.152(1)	0.696(1)	1.967(1)	4.596(1)	0.010(1)	-0.005(1)	0.011(1)	-14.4
$d_{\mathrm{Ni-Ni}}$ Å	4.405	4.889	6.072	6.112	6.114	8.116	8.387	8.563	

Supplementary Table 2. Exchange interactions of $K_2Ni_2(SO_4)_3$, calculated for six different values of the on-site interaction strength U. The line in boldface is interpolated to yield the experimental value of the Curie-Weiss temperature (Ref. [S1]), using Eq. (1). Statistical errors from the fitting procedure are given.

strength U; the Hund's rule coupling was fixed to $J_\mathrm{H} = 0.88\,\mathrm{eV}$ following Ref. [S2]. The long-range couplings J_6 to J_8 turn out to be very close to zero; they are listed in Supplementary Table 2 but not shown in Supplementary Fig. 2. Note that resolving these small long-range couplings is not irrelevant because, on the one hand, we find proof that they do not play a role as opposed to just assuming this is the case. On the other hand, resolving fewer exchange interactions in the energy mapping procedure has the consequence that long-range couplings are added into short-range couplings with some prefactor – this is only harmless if the long-range couplings are really effectively zero. Note that between room temperature and $T = 100\,\mathrm{K}$ structure, J_4 and J_5 would switch places if we strictly number exchange couplings by Ni-Ni distance. Therefore, as can be seen in Supplementary Table 2, we use the name J_5 for the second trillium coupling and J_4 for the dominant coupling connecting trillium lattices also in the low-temperature structure. In this way, we can see that cooling the lattice of $K_2Ni_2(SO_4)_3$ leads to moderate but, as we demonstrate in the main text, significant adjustments in the Heisenberg Hamiltonian parameters. We choose the relevant value of the interaction U by demanding that the set of interactions match the experimental Curie-Weiss temperature of $\theta_\mathrm{CW} = -18$ K. From the Heisenberg exchange interactions, we determine the Curie-Weiss temperature according to

$$\theta_\mathrm{CW} = -\frac{1}{3}S(S+1)\big(J_1 + 3J_2 + 3J_3 + 3J_4 + 3J_5 + 3J_6 + 3J_7 + 3J_8\big)\,, \tag{1}$$

where $S = 1$.

Supplementary Note 3. CMC THERMODYNAMICS

We perform classical Monte Carlo calculations on systems of $N = 8 \times L^3$ classical unitary spins, with different sizes L from 2 ($N = 64$) and up to 12 ($N = 13824$). Generally, a logarithmic cool down with 150 steps is applied from $T = 2.0\ J_4$ down to $0.001\ J_4$ (a finer grid can be applied later to any particular region of interest, e. g. a phase transition). At each temperature, 10^5 Monte Carlo steps are applied, each consisting of N single-site Metropolis trials and N over-relaxation updates (intercalated). We also fix the acceptance ratio of the Metropolis trial close to 50% by using the so-called Gaussian step [S3]. Data for the calculation of the energy e and specific heat c_v are collected during the second half of the Monte Carlo steps at each temperature and later averaged over 5 independent runs.

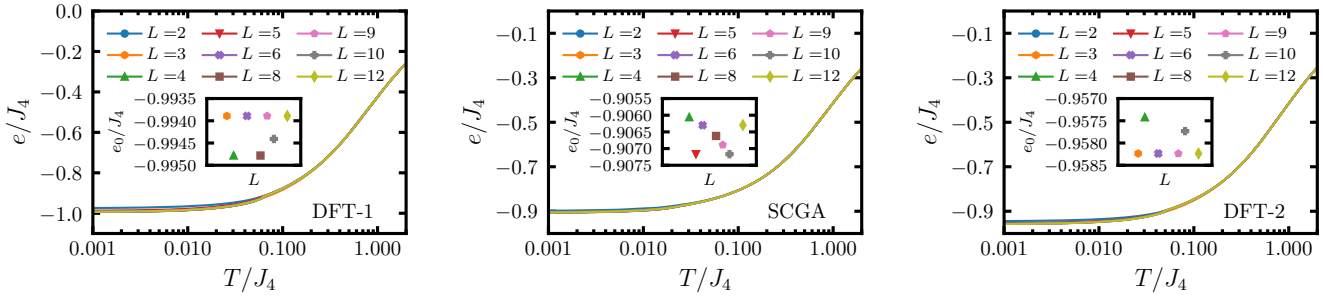

Supplementary Figure 3. Energy as a function of T/J_4 for three different models of $K_2Ni_2(SO_4)_3$: DFT-1 [S1], SCGA [S4], and DFT-2 corresponding to the updated structure and parameters presented in this article. Insets show the ground-state energy obtained in the $T \to 0$ limit, depending on the lattice size L.

Supplementary Figure 3 shows the results of $e/J_4(T)$ for the three different models: the DFT model from Ref. [S1] (DFT-1, left), the SCGA model from Ref. [S4] (middle), and the new DFT model presented in this article taking into account the 100 K structure (DFT-2, right). Phase transitions can be seen as very small features in each curve, showing the highly frustrated nature of the models. The inset in each panel shows the ground-state energy obtained in the limit $T \to 0$ as a function of the size L. For DFT-1, the lowest energy is obtained for the $L = 4n$ lattices. However, $L = 12$ converges to the $L = 3n$ energy, a little above. Since $L = 12$ can fit the $L = 4$ solution which has lower energy, a transition should occur from one state to the other. However, orders are complicated and different from one another, so that $L = 12$ gets trapped in a stable excited state. For SCGA, the lowest energy is obtained for $L = 5n$, and the $L = 3n$ observed experimentally is not observed. For the new DFT-2 model, the lowest energy is found for $L = 3n$. In this case, $L = 8$ gets trapped in a higher energy state, but it should be in the same line as $L = 4$ at least.

Supplementary Note 4. PFFRG FLOWS

The PFFRG method [S5] relies on writing the quantum spin operators in terms of $S = 1/2$ fermionic operators. Using many-body Feynman diagrammatic techniques and introducing an infrared frequency cutoff Λ leads to an infinite set of coupled differential equations for the corresponding fermionic vertex functions, from which the spin-spin correlations at $T = 0$ can be obtained by choosing an appropriate truncation scheme. In this case, we use the one-loop approximation to resolve the flow in real space, starting from known initial conditions at $\Lambda \to \infty$. Most importantly, PFFRG contains the correct large-N and large-S limits [S6, S7]. This means that the PFFRG equations can be generalized for a Heisenberg model with SU(N) symmetry, where N is the number of flavours, and they become exact in the limit $N \to \infty$. On the other hand, the PFFRG equations can also be extended for arbitrary spin-S systems, and in the limit of $S \to \infty$ they can be solved analytically to obtain the exact classical results. These exact properties at large N and large S are still important in our current situation where $S = 1$ and $N = 2$ take finite values. Specifically, a strongly magnetically ordered phase at finite S behaves similar to a classical magnet, which implies that such phases can be well described by the classical limit $S \to \infty$ (e.g. spin mean-field theory provides a good description in such phases). Hence, with the exact inclusion of all $S \to \infty$ diagrammatic contributions in PFFRG, this approach is well capable of describing strongly magnetically ordered phases. A similar argument applies to the large N limit where a quantum system typically becomes non-magnetic, e.g. it is a valence-bond solid or a quantum spin liquid. A system deep in such a non-magnetic phase can therefore be expected to be well described by a model at large N (e.g. in a so-called parton-mean field theory [S8]). This implies that due to the inclusion of all $N \to \infty$ diagrammatic contributions, the PFFRG is also expected to be well capable of describing strongly disordered

phases. On the other hand, the critical regions where both phases meet can be challenging, which explains the large regions of uncertainty in the phase diagram from PFFRG in Fig. 4a in the main text.

In practice, higher values of $S > 1/2$ are obtained by coupling copies of the $S = 1/2$ fermionic spins at each site [S6] (in the present case for $S = 1$ only two are needed).

In particular, since PFFRG preserves all symmetries of the original Hamiltonian, the onset of magnetic order (symmetry breaking) is signalled by a breakdown in the Λ flow. This means that a peak or kink appears in the susceptibility as a function of Λ. When this is the case, the results cannot be trusted at lower values of Λ, and the usual practice is to calculate the spin-spin correlations at the point (or a little above) where the flow breaks. This does not need to be very precise, as the results do not change qualitatively very close to the breaking point. On the other hand, if there is no magnetic order (all symmetries are preserved), the flow continues smoothly down to $\Lambda \ll J_4$. We also exploit the translation symmetry of the lattice and calculate spin-spin correlations only up to a certain distance from the reference sites (those not connected by lattice symmetries). In this case, we take distances up to 3 unit cells, implying 1842 lattice vectors that can be reduced to 622 after exploiting the lattice symmetries.

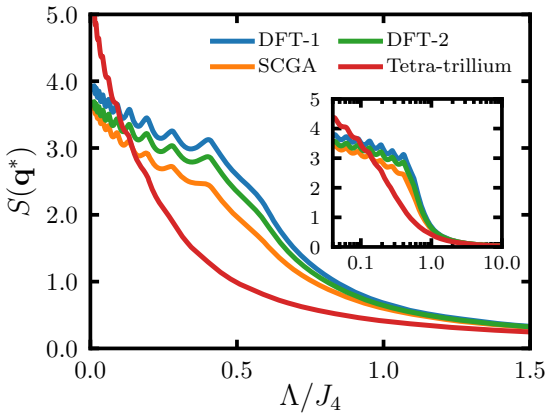

Supplementary Figure 4. PFFRG flows for different models. For each case, $\mathbf{q}^*$ corresponds to the point in reciprocal space for which the highest value of the spin structure factor is observed.

Supplementary Figure 4 shows examples of Λ-flows for the DFT-1, DFT-2, SCGA, and tetra-trillium models. For the first three, a breakdown is clearly observed, indicating some kind of symmetry breaking in the ground state of the corresponding models. On the other hand, the flow of the tetra-trillium lattice continues to the lowest values of Λ without presenting any peaks or kinks, indicating no symmetry breaking in this case. For each case, $\mathbf{q}^*$ corresponds to the point in reciprocal space for which the highest value of the spin structure factor is observed in the low cutoff limit (also for the flows with breakdown).

Supplementary Note 5. SPIN STRUCTURE FACTOR FOR OTHER MODELS

The cMC data for the correlations are calculated separately from an already thermalized configuration at a given temperature T, by doing 4×10^5 Monte Carlo steps while measuring once every 10^2, averaging over 5 independent runs. The results are shown in Supplementary Fig. 5, along with the PFFRG calculations. The first two rows correspond to the DFT-1 and SCGA models [S1, S4], respectively. For these, cMC calculations are performed at $T = 0.3\ J_4$ and PFFRG calculations are performed at the point where the Λ-flow breaks. The quantum-to-classical correspondence phenomenon is observed in both cases. The last row corresponds to the tetra-trillium lattice, where there is no breakdown of the flow in PFFRG. Therefore, correlations can be calculated at the lowest $\Lambda = 0.01 J_4$. When these results are compared against cMC calculations at low temperatures (top quadrants of the bottom panels), there is no agreement between the patterns. This indicates that the quantum and classical liquid ground states are fundamentally different. The quantum-to-classical correspondence is only recovered at finite T and Λ, as shown in the lower parts of the last row of panels.

The striking resemblance between quantum and classical correlations at different temperatures has already been studied in Heisenberg models [S9]. In Ref. [S9], the authors focused on a mapping of exchange interactions and temperature between the quantum and classical models to obtain a quantitatively accurate correspondence. In our present case, we only allowed temperature in cMC calculations to be varied, with exchange parameters kept fixed. This quantum-to-classical correspondence indicates a mapping between the quantum $S = 1$ calculations at finite renormalization group parameter Λ and classical calculations at finite temperature T. It hints that quantum

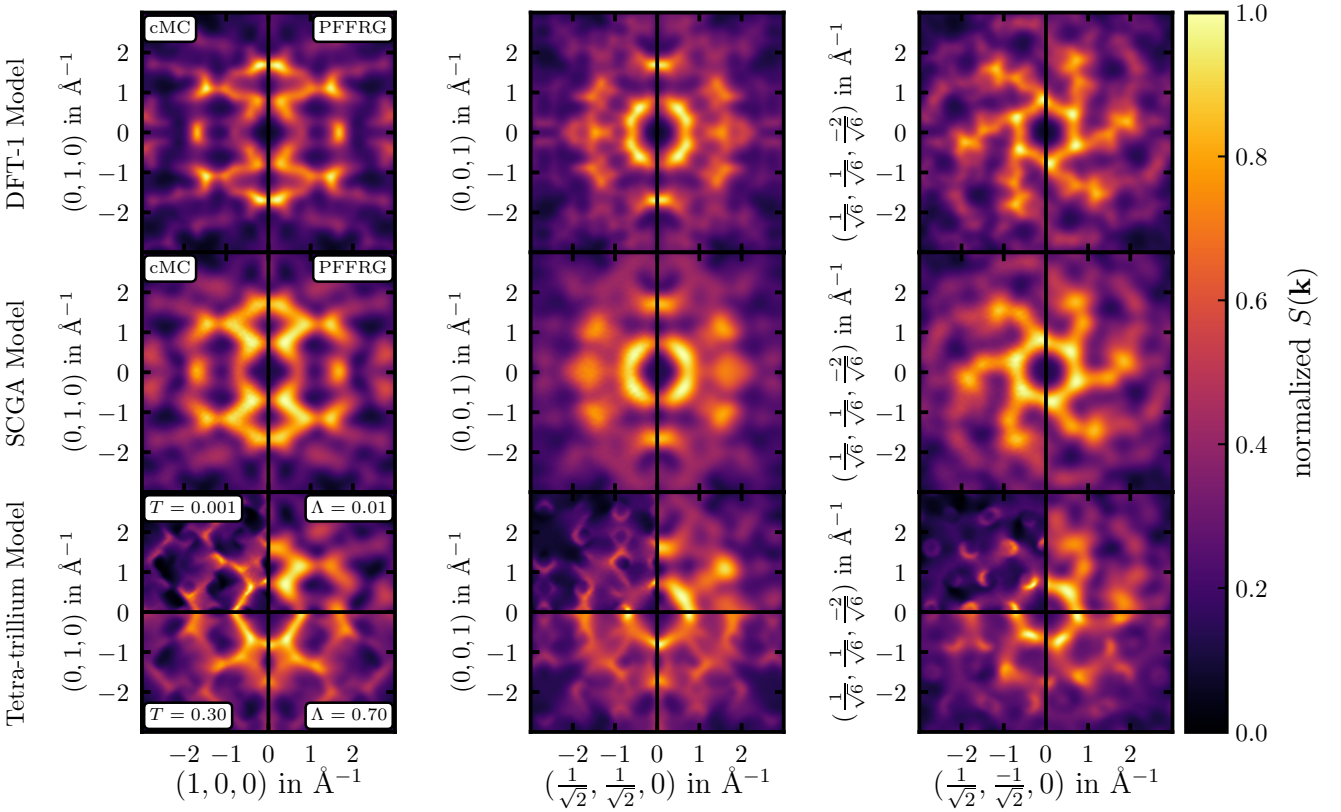

Supplementary Figure 5. Spin structure factor obtained with cMC (left parts) and PFFRG (right parts). The first two lines correspond to DFT-1 [S1] and SCGA models [S4], and calculations are at $T = 0.3J_4$ for cMC and at the breaking point of the flow for PFFRG. The bottom row corresponds to the tetra-trillium lattice, and temperatures and Λ-cutoffs are indicated in the panels.

fluctuations can be well reproduced by thermal fluctuations at finite temperatures. Finally, the quantum-to-classical correspondence has already been observed to find a limit of validity when the temperature of the quantum solution is lowered and quantum fluctuations start playing a stronger role, even when trying to change the set of parameters from quantum to classical models [S9].

Supplementary Note 6. GROUND STATE OF THE TETRA-TRILLIUM LATTICE

As mentioned in the main article, classical ground-state spin configurations for the tetra-trillium lattice can be easily found. In Supplementary Fig. 6a, a simple configuration is shown where blue and red sites correspond to two opposite directions for spins (up and down, such that it can also be a ground state of the Ising model). In this particular configuration, half of the spins in each lattice point up, and the remaining half point down. Thus, both sublattices have total zero magnetization. We have verified numerically that the configuration defined on a single unit cell can be copied throughout the whole lattice and the ground-state energy is obtained. We show in Supplementary Fig. 6b a larger part of the lattice, but only taking into account the J_5 trillium sublattice lattice. In this sublattice, a loop of 9 spins can be defined as shown by the yellow paths, consisting of two pentagons and one triangle that share a common base. Flipping the 9 spins in this loop leaves all triangles in the trillium sublattice with two spins pointing in one direction and the third in the other. This means, no triangles are left with three spins pointing in the same direction. Therefore, the zero-sum in each tetrahedron can be satisfied by choosing accordingly the spin on the J_3 trillium sublattice. This is shown in Supplementary Fig. 6c, where the remaining 9 spins are connected to the yellow loop by light-blue lines. This total of 18 spins can be flipped while maintaining the ground-state energy. We have verified that these loops can be found systematically departing from any site. Flipping an 18-spin cluster leads to a non-periodic ground state. We have found that in non-periodic ground states one can find smaller clusters to flip. However, a detailed explanation will be presented elsewhere.

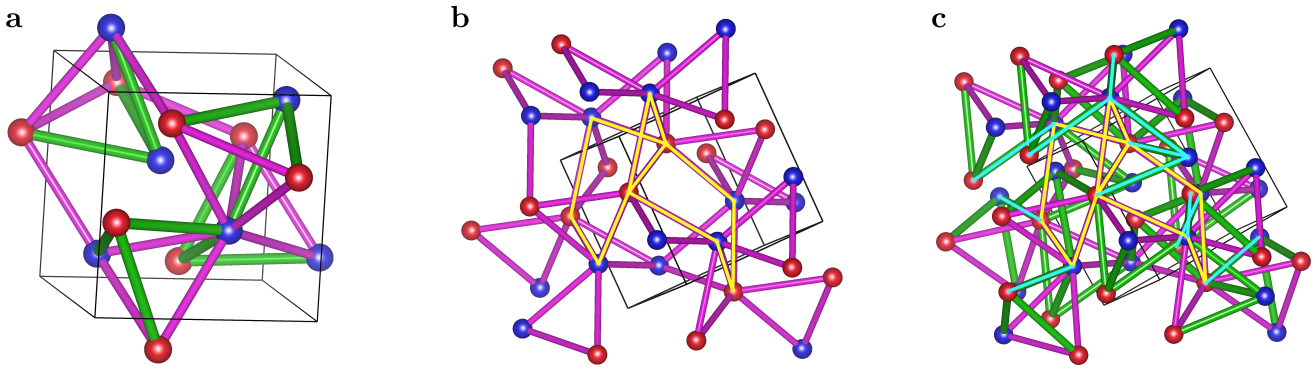

Supplementary Figure 6. (a) one possible ground-state configuration defined in one unit cell. (b) flippable loop on the J_5 trillium lattice. (c) flippable loop on the tetra-trillium lattice.

[S1] I. Živković, V. Favre, C. Salazar Mejia, H. O. Jeschke, A. Magrez, B. Dabholkar, V. Noculak, R. S. Freitas, M. Jeong, N. G. Hegde, L. Testa, P. Babkevich, Y. Su, P. Manuel, H. Luetkens, C. Baines, P. J. Baker, J. Wosnitza, O. Zaharko, Y. Iqbal, J. Reuther, and H. M. Rønnow, Magnetic Field Induced Quantum Spin Liquid in the Two Coupled Trillium Lattices of $K_2Ni_2(SO_4)_3$, Phys. Rev. Lett. **127**, 157204 (2021).

[S2] T. Mizokawa and A. Fujimori, Electronic structure and orbital ordering in perovskite-type $3d$ transition-metal oxides studied by Hartree-Fock band-structure calculations, Phys. Rev. B **54**, 5368 (1996).

[S3] J. D. Alzate-Cardona, D. Sabogal-Suárez, R. F. L. Evans, and E. Restrepo-Parra, Optimal phase space sampling for Monte Carlo simulations of Heisenberg spin systems, J. Phys. Condens. Matter **31**, 095802 (2019).

[S4] W. Yao, Q. Huang, T. Xie, A. Podlesnyak, A. Brassington, C. Xing, R. S. D. Mudiyanselage, H. Wang, W. Xie, S. Zhang, M. Lee, V. S. Zapf, X. Bai, D. A. Tennant, J. Liu, and H. Zhou, Continuous spin excitations in the three-dimensional frustrated magnet $K_2Ni_2(SO_4)_3$, Phys. Rev. Lett. **131**, 146701 (2023).

[S5] J. Reuther and P. Wölfle, J_1-J_2 frustrated two-dimensional Heisenberg model: Random phase approximation and functional renormalization group, Phys. Rev. B **81**, 144410 (2010).

[S6] M. L. Baez and J. Reuther, Numerical treatment of spin systems with unrestricted spin length S: A functional renormalization group study, Phys. Rev. B **96**, 045144 (2017).

[S7] F. L. Buessen, D. Roscher, S. Diehl, and S. Trebst, Functional renormalization group approach to SU(N) Heisenberg models: Real-space renormalization group at arbitrary N, Phys. Rev. B **97**, 064415 (2018).

[S8] I. Affleck and J. B. Marston, Large-n limit of the Heisenberg-Hubbard model: Implications for high-T_c superconductors, Phys. Rev. B **37**, 3774 (1988).

[S9] T. Wang, X. Cai, K. Chen, N. V. Prokof'ev, and B. V. Svistunov, Quantum-to-classical correspondence in two-dimensional Heisenberg models, Phys. Rev. B **101**, 035132 (2020).